International Journal of Heat and Technology
Vol. 43, No. 5, October, 2025, pp. 1877-1890
Journal homepage: http://iieta.org/journals/ijht

Multiscale Heat Transfer and Thermodynamic Constraint Modeling of Explosion-Induced Thermal Wave Propagation in Smart Cities

Fangzhou He[1*], Zhiqi Wang[2]

[1] School of Public Security Information Technology and Intelligence, Criminal Investigation Police University of China, Shenyang 110854, China
[2] School of Investigation and Counter-Terrorism, Criminal Investigation Police University of China, Shenyang 110854, China

Corresponding Author Email: hefangzhou963@126.com

https://doi.org/10.18280/ijht.430527

Received: 19 February 2025
Revised: 8 July 2025
Accepted: 12 September 2025
Available online: 31 October 2025

Keywords:
smart city, explosion-induced thermal wave, multiscale heat transfer, thermodynamic constraints, numerical simulation

ABSTRACT

High-density building clusters and complex urban pipeline networks in smart cities cause explosion-induced thermal waves to exhibit strongly nonlinear and tightly coupled propagation behavior. Existing models fail to achieve accurate prediction because the cross-scale mechanisms governing heat transfer—from the macro to the meso and micro levels—have not been quantitatively characterized and the absence of thermodynamic constraints leads to deficiencies in physical consistency. To address these limitations, a systematic investigation was conducted in this study. First, the cross-scale energy-transfer pathways involving macroscopic regional convective–diffusive processes, mesoscopic porous fluid–solid thermal coupling, and microscopic molecular heat conduction were elucidated, and quantitative formulations for scale-coupling coefficients and heat-transfer contribution ratios were established. Second, a thermodynamic constraint framework rooted in the laws of energy conservation and entropy production was constructed, into which scenario-specific boundary conditions—such as building thermal properties and medium distributions within pipeline networks—were embedded to develop a unified multiscale predictive model. Third, an integrated multiscale solver combining an improved finite-volume method (FVM), the lattice Boltzmann method (LBM), and molecular dynamics (MD) was proposed, and a deep-learning surrogate model was incorporated to enhance mesoscopic–microscopic computational efficiency, thereby overcoming the conventional trade-off between accuracy and efficiency. Finally, dual validation was achieved through shock-tube experiments and field measurements from an industrial-park explosion case. This study provides a physically rigorous and operationally practical theoretical framework for emergency early warning and safety planning in smart-city high-risk events.

1. INTRODUCTION

Driven by accelerated global urbanization, smart cities have emerged as a central paradigm in urban development. The coexistence of high-density building clusters, complex pipeline networks, and the close spatial arrangement of high-risk zones such as chemical industrial parks and energy hubs [1-4] has caused explosion-induced thermal waves to exhibit strongly nonlinear characteristics, including multipath reflection, cross-medium coupling, and disaster-chain amplification. These features pose severe challenges for urban emergency management. Recent urban explosion incidents have shown that thermal waves refracted through building gaps or transmitted along pipeline networks can cause extensive damage to remote areas [5, 6], revealing substantial deviations in traditional predictive models when applied to complex urban environments. High-accuracy modeling is therefore urgently required to support emergency decision-making and safety planning. Fundamentally, the propagation of explosion-induced thermal waves represents a highly complex process involving multiscale heat-transfer interactions across macroscopic, mesoscopic, and microscopic domains, together with coupled thermal–fluid–solid multiphysics effects [7, 8]. The macroscopic scale involves thermal convection and diffusion within urban spaces [9]; the mesoscopic scale involves fluid–solid thermal coupling within porous building structures and pipeline networks [10]; the microscopic scale involves energy transport governed by molecular heat conduction and lattice vibrations [11]. However, conventional modeling approaches typically rely on single-scale formulations and emphasize energy conservation while neglecting the thermodynamic constraints imposed by entropy production. As a result, non-physical behaviors such as temperature backflow frequently arise, preventing these models from achieving the predictive accuracy required in smart-city scenarios [12, 13]. Moreover, advances in modeling explosion-induced thermal-wave propagation hold direct relevance to the United Nations Sustainable Development Goal of building inclusive, safe, and resilient cities [14], granting this research both substantial engineering significance and foundational disciplinary value.

Current research on multiscale heat transfer has evolved into a domain characterized by scale-segmented investigations. At the macroscopic level, computational fluid dynamics (CFD) methods are primarily employed to analyze the influence of building density on the spatial extent of thermal diffusion; however, disturbances induced by mesoscopic pore structures are not incorporated, nor is the heat-transfer enhancement associated with urban pipeline systems adequately represented [15, 16]. At the mesoscopic level, the LBM has been widely used to simulate coupled thermal convection and conduction within porous media, yet the heterogeneity of urban construction materials and the stochasticity of pipeline layouts have not been appropriately captured, resulting in boundary conditions that lack scenario specificity [17, 18]. At the microscopic level, MD has revealed the microscopic origins of thermal conductivity and clarified energy-transport mechanisms governed by molecular collisions and lattice vibrations, but no quantitative linkage with macroscopic propagation processes has been established. Consequently, the efficiency of cross-scale energy transfer and the coupling coefficients between scales remain insufficiently characterized [19, 20]. Research focused on modeling explosion-induced thermal-wave propagation faces similarly pronounced limitations. Empirical formulations, such as the multi-energy method, offer computational efficiency but remain applicable only to open spaces and perform poorly under complex urban boundaries involving building shielding or intersecting pipeline networks [21]. Numerical simulation methods provide greater detail but typically neglect scenario-specific parameters of urban environments or consider only energy conservation while omitting thermodynamic constraints associated with entropy production [22]. With respect to solution algorithms, conventional numerical schemes—such as the finite element method and FVM—experience severe efficiency bottlenecks, since computational demand increases dramatically as grid refinement is used to resolve microscale features, often approaching exponential growth [23, 24]. Data-driven approaches, including deep-learning-based surrogate models, can accelerate computation but lack underlying physical mechanisms, preventing them from satisfying the reliability requirements of emergency-response applications [25].

Overall, three fundamental gaps persist in existing research. At the mechanistic level, the coupled multiscale energy-transfer behavior of explosion-induced thermal waves in smart-city environments has not been clarified. The cross-scale pathways linking macroscopic, mesoscopic, and microscopic processes remain indistinct, and key parameters such as coupling coefficients have not been quantitatively expressed, preventing the determination of scale-dependent contribution weights within the overall propagation behavior. At the modeling level, no integrated constraint framework combining the fundamental laws of thermodynamics with smart-city scenario-specific environments has been established. Boundary conditions largely rely on empirical assumptions, producing models that fail to ensure physical consistency and lack sufficient adaptability to complex urban settings. At the methodological level, no solution strategy has been developed that simultaneously satisfies the accuracy and efficiency requirements inherent to multiscale modeling. Both traditional numerical methods and data-driven techniques exhibit intrinsic limitations and are unable to meet the smart-city demands for simultaneous real-time responsiveness, predictive accuracy, and reliability.

In response to the aforementioned gaps, a systematic investigation was conducted with four core objectives: to elucidate the coupled mechanisms governing macroscopic–mesoscopic–microscopic multiscale heat transfer during explosion-induced thermal-wave propagation in complex smart-city environments and to quantify the contribution ratios associated with each scale; to establish a multiscale predictive model integrating thermodynamic constraints and scenario-specific urban boundary conditions, thereby eliminating non-physical behaviors observed in traditional models; to develop a hybrid solution strategy that combines physics-based mechanisms with data-driven components, enabling the unified achievement of accuracy and computational efficiency; and to validate model reliability through both controlled experiments and real-world disaster cases, ultimately forming an actionable application framework. The academic contributions of the study are reflected in four major aspects. First, the cross-scale coupling mechanisms regulated by heterogeneous smart-city boundaries are identified for the first time, and a quantitative methodology for determining coupling coefficients based on energy-transfer efficiency is proposed, clarifying the distribution patterns of macroscopic convection, mesoscopic coupling, and microscopic conduction contributions. Second, a thermodynamic-constraint system integrating energy conservation, entropy production, and scenario-specific boundaries is constructed, and building thermal-property tensors together with state equations of pipeline media are incorporated to fundamentally ensure physical consistency within the model. Third, an integrated “FVM–LBM–MD” multiscale coupling framework is developed, in which a deep-learning surrogate model is introduced to replace portions of the direct mesoscopic–microscopic simulations, significantly improving computational efficiency while preserving underlying physical mechanisms. Fourth, a dual validation system combining shock-tube experiments with real-world industrial explosion cases is established, covering varying explosion intensities, building configurations, and pipeline distributions, thereby providing comprehensive verification of applicability and stability.

The study is structured around a closed-loop logic of mechanism analysis → model construction → algorithm development → validation and application. Initially, the single-scale behaviors and cross-scale coupling mechanisms governing multiscale heat transfer in explosion-induced thermal-wave propagation are systematically analyzed, and criteria for scale delineation together with the characteristics of coupling interfaces are defined. Subsequently, a constraint framework based on the fundamental laws of thermodynamics is formulated, scenario-specific parameters characteristic of smart-city environments are embedded, and unified multiscale governing equations along with initial and boundary conditions are derived. The implementation of the hybrid solution algorithm is then presented, including the logical coupling between scale-specific solvers, surrogate-model training strategies, and convergence-optimization procedures. High-precision experimental data are later obtained through shock-tube measurements, and model accuracy is evaluated both quantitatively and qualitatively using an explosion case from a representative chemical industrial park. Finally, the physical implications of the results, distinctions and limitations relative to existing studies, and directions for future development—particularly the integration of digital-twin technologies to enable dynamic early-warning capabilities—are discussed, forming a complete theoretical and application-oriented framework.

2. MULTISCALE HEAT TRANSFER MECHANISMS GOVERNING EXPLOSION-INDUCED THERMAL WAVE PROPAGATION

The propagation of explosion-induced thermal waves in smart-city environments represents a continuous process of cross-scale energy transfer and transformation. The delineation of scales must satisfy the simultaneous compatibility of spatial scales, temporal scales, and dominant physical processes. Based on these criteria, a three-scale system—macroscopic, mesoscopic, and microscopic—was defined. The macroscopic scale encompasses urban regions on the order of 10^0–10^3 m, with characteristic time scales ranging from seconds to minutes. The dominant physical processes at this scale involve thermal wave convection and diffusion within high-density building clusters and complex pipeline networks. Key governing factors include building spatial density, atmospheric turbulence intensity, and pipeline-network topology, all of which act as macroscopic boundary conditions. Thermal waves exhibit collective propagation behaviors such as diffraction, reflection, and superposition at this scale. The mesoscopic scale spans localized regions on the order of 10^{-3}–10^0 m, with millisecond to second time scales. This scale corresponds to coupled flow–thermal fields within porous architectural materials and near-wall regions of underground pipeline systems. The essential physical processes involve coupled thermal convection within porous media and thermal conduction through the solid skeleton. Permeability and pore-structure geometry are the critical parameters regulating mesoscopic heat-transfer efficiency. The microscopic scale targets molecular and lattice domains on the order of 10^{-9}–10^{-3} m, with characteristic time scales of nanoseconds to microseconds. At this scale, molecular collisions, lattice vibrations, and phonon transport dominate the thermal-conduction process. Intermolecular forces and material crystalline structure directly determine microscopic heat-transfer capacity. These three scales are not independent; instead, they interact through a hierarchical cascade of energy transfer, forming a sequence of “microscopic energy accumulation → mesoscopic energy amplification → macroscopic energy dispersion.”

The underlying heat-transfer mechanisms at each scale exhibit distinct characteristics, and their governing principles and quantitative descriptors can be precisely formulated through physics-based models. At the macroscopic scale, heat transfer is dominated by thermal convection, supplemented by thermal radiation, and must be captured through macroscopic fluid-mechanics governing equations. An effective-porosity correction is required to represent building shielding effects. The continuity, momentum, and energy equations can be expressed as follows:

$$\begin{aligned} &\frac{\partial \rho}{\partial t} + \nabla\cdot\left(\rho\tilde{u}\right) = 0 \\ &\rho\left(\frac{\partial \tilde{u}}{\partial t} + \tilde{u}\cdot\nabla\tilde{u}\right) = -\nabla p + \mu\nabla^2\tilde{u} + \rho\tilde{g} \\ &\rho c_p\left(\frac{\partial T}{\partial t} + \tilde{u}\cdot\nabla T\right) = \nabla\cdot\left(k\nabla T\right) + q \end{aligned} \tag{1}$$

where, ρ denotes the density of the thermal-wave medium, $\tilde{u}$ denotes the propagation velocity, p denotes the pressure, μ denotes the dynamic viscosity, c_p denotes the specific heat capacity at constant pressure, k denotes the macroscopic thermal-conductivity coefficient, and q denotes the explosion-induced thermal source term. Scenario-specific adaptation is achieved by introducing a building-distribution correction factor ϕ, which modifies k and μ accordingly. At the mesoscopic scale, heat transfer exhibits strong coupling between thermal convection and thermal conduction. The flow field within porous structures is therefore described using the Brinkman equation, while the solid–fluid thermal coupling is represented through an effective-thermal-conductivity model expressed as $k_{\text{eff}}=k_s\cdot(1-\varepsilon)+k_f\cdot\varepsilon\cdot f(\varepsilon,Re)$, where k_s and k_f denote the thermal conductivities of the solid skeleton and fluid medium, respectively, ε represents porosity, Re is the pore-scale Reynolds number, and $f(\varepsilon,Re)$ is a coupling correction function. This function exhibits an approximately linear relationship when $Re < 10$ and approaches a constant value when $Re > 100$. At the microscopic scale, heat transfer is dominated by molecular thermal conduction. Based on the MD theory, heat transport originates from energy exchange during inelastic molecular collisions and from phonon propagation induced by lattice vibrations. Intermolecular interactions are described using the Lennard–Jones potential, and thermal conductivity is quantified through the Green–Kubo relation:

$$k = \frac{1}{3Vk_BT^2}\int_0^\infty \left\langle J(0)\cdot J(t)\right\rangle dt \tag{2}$$

where, V represents the system volume, k_B represents the Boltzmann constant, and $\langle J(0)\cdot J(t)\rangle$ represents the heat-flux autocorrelation function. Lattice defects induce phonon scattering, typically reducing thermal conductivity by approximately 15–30%.

The cross-scale coupling mechanism serves as the central linkage connecting the three scales, and its formulation relies on the explicit identification of coupling interfaces, transfer pathways, and quantitative coefficients. The microscopic–mesoscopic coupling interface corresponds to the contact surface between the solid skeletal structure of the material and the pore-scale fluid. The associated energy-transfer pathway follows the sequence “microscopic molecular vibrational energy → lattice conduction within the solid skeleton → interfacial heat-flux transfer → mesoscopic pore-fluid convection.” The coupling strength is quantified by an interfacial heat-flux coupling coefficient α, defined as $\alpha=q_{\text{int}}/(T_m-T'_m)$, where q_{int} denotes the interfacial heat-flux density, Tm denotes the microscopic solid-surface temperature, and $T'm$ denotes the mesoscopic fluid temperature. Typical values fall within 10^4–10^6 W/(m²·K) and increase significantly with surface roughness. The mesoscopic–macroscopic coupling interface is located at the contact region between building exterior walls and the urban atmosphere. Energy transfer occurs through the aggregation of pore-scale thermal fluxes into the macroscopic thermal-wave front. An energy-transfer efficiency coefficient β is introduced, defined as $\beta=Q_{\text{mac}}/Q_{\text{mes}}$, where Q_{mac} represents the macroscopic energy output and Q_{mes} represents the mesoscopic accumulated energy. β exhibits a negative correlation with wall thickness; an increase of 0.1 m typically reduces β by approximately 5–8%. The influence of coupling effects on thermal-wave propagation can be quantified through numerical simulation. When cross-scale coupling is not considered, prediction errors in macroscopic peak temperature reach 22–35%, and errors in propagation velocity reach 18–28%. After incorporating coupling coefficients, these deviations are reduced to 4.5–6.8% and 3.2–5.1%, respectively. Moreover, the cross-scale coupling mechanism enhances the attenuation rate of the thermal wave within building clusters by 15–22% and effectively suppresses non-physical behaviors such as temperature backflow. The clarification of this coupling mechanism therefore provides essential theoretical support for unified multiscale modeling.

3. THERMODYNAMIC CONSTRAINT MODELING

3.1 Fundamental thermodynamic principles

The fundamental laws of thermodynamics constitute the core framework that ensures the physical consistency of multiscale modeling for explosion-induced thermal waves. Within this framework, the conservation of energy, the principle of entropy production, and the conservation of mass jointly provide a tripartite set of constraints that must be tightly coupled with the multiscale characteristics of thermal transport. The conservation of energy mandates that, throughout the propagation of an explosion-induced thermal wave, the total amount of thermal energy produced by chemical-energy conversion remains conserved across the macroscopic, mesoscopic, and microscopic scales. Energy can neither be created nor destroyed; it can only be transformed between different forms or transferred from one scale to another. This law provides the foundational basis for quantifying multiscale thermal transport and ensures that the computational representation of heat-flux density and temperature fields remains consistent with energy conservation. The principle of entropy production governs all irreversible processes and imposes an essential constraint on thermal-wave propagation. As a representative irreversible process, the total entropy change of the system must be greater than or equal to zero. Entropy production originates from temperature gradients driving thermal conduction, viscous dissipation arising from fluid motion, and energy dissipation at cross-scale coupling interfaces. This principle fundamentally prevents the emergence of non-physical behaviors frequently observed in traditional models, such as temperature backflow and energy transfer without dissipation. The conservation of mass provides an additional constraint by ensuring that the mass of the thermal-wave carrier medium remains conserved during propagation. Across macroscopic convective–diffusive transport, mesoscopic pore-scale flow, and microscopic molecular motion, variations in mass concentration are governed solely by transport processes. This constraint provides a fundamental constraint for the coupled modeling of heat transfer and fluid flow. Together, these three principles form an interdependent “energy–entropy–mass” thermodynamic framework. Their coordinated application guarantees that the multiscale model maintains physical validity during scale bridging and parameter transfer.

3.2 Construction of thermodynamic constraint equations

The formulation of the energy-conservation constraint must incorporate the multiscale characteristics of thermal transport. A unified multiscale expression can be derived from the first law of thermodynamics, and its general form is expressed as:

$$\rho c_p \frac{\partial T}{\partial t} + \rho c_p \tilde{u} \cdot \nabla T = \nabla \cdot \left(k_{eff} \nabla T \right) + q_{rad} + q_{src} \tag{3}$$

where, ρ denotes the density of the medium. At the macroscopic scale, the density of air (1.2 kg/m^3) is adopted; at the mesoscopic scale, an effective density is used, denoted as $\rho_{\text{eff}}=\rho_s(1-\varepsilon)+\rho f\varepsilon$; at the microscopic scale, the equivalent density corresponds to the molecular number density. The specific heat capacity at constant pressure c_p varies dynamically with temperature—for instance, c_p of concrete increases from approximately 900 J/(kg·K) to 1200 J/(kg·K) across 20–1000°C. T denotes temperature, and t denotes time. The velocity field u corresponds to the thermal-wave propagation velocity at the macroscopic scale, the pore-fluid velocity at the mesoscopic scale, and the averaged thermal motion of molecules at the microscopic scale. The effective thermal conductivity k_{eff} is determined differently across scales: at the macroscopic scale, it is derived from the combined contributions of air conduction and equivalent radiative conductivity associated with urban building envelopes; at the mesoscopic scale, it is computed using the ε-Kruger model; at the microscopic scale, it is calculated using the Green–Kubo relation from the MD theory. The radiative heat-transfer term q_{rad} is evaluated at the macroscopic scale using the Stefan–Boltzmann law, $q_{\text{rad}}=\sigma\varepsilon_{\text{surf}}(T^4-T^{04})$, in which σ is the Stefan–Boltzmann constant and $\varepsilon_{\text{surf}}$ is the emissivity of the building surface. Radiative effects at the mesoscopic and microscopic scales are negligible due to scale limitations. The explosion heat-source term q_{src} is obtained from the Jones–Wilkins–Lee (JWL) equation of state, which characterizes the energy release of detonation products:

$$q_{src} = \frac{1}{V}\left(A\left(1-\frac{\omega}{R_1 V}\right)e^{-R_1 V} + B\left(1-\frac{\omega}{R_2 V}\right)e^{-R_2 V} + \omega E_0 \right) \tag{4}$$

where, A, B, R_1, and R_2 are material-specific parameters of the explosive, V is the relative specific volume, and E_0 is the initial internal energy. Through the multiscale adaptation of k_{eff} and u, Eq. (4) provides a unified representation of energy conservation across multiscale heat transport.

The entropy-production constraint is introduced to quantify the irreversibility of the process, and a multiscale entropy equation can be derived from the second law of thermodynamics:

$$\rho c_p \frac{\partial(\ln T)}{\partial t} - \nabla \cdot \left(\frac{k_{eff} \nabla T}{T} \right) = \frac{\dot{S}_{gen}}{T} + \frac{q_{src}}{T} \tag{5}$$

where, $\dot{S}_{\text{gen}}$ denotes the volumetric entropy-production rate, which is strictly non-negative and constitutes the key term that suppresses non-physical behavior. The entropy production is composed of three components: the entropy production associated with heat conduction $\dot{S}_{\text{gen,cond}}$, the viscous-dissipation entropy production of fluid flow $\dot{S}_{\text{gen,vis}}$, and the cross-scale coupling entropy production $\dot{S}_{\text{gen,couple}}$. These components can be expressed as:

$$\begin{aligned} \dot{S}_{gen,cond} &= \frac{k_{eff}\left(\nabla T\right)^2}{T^2} \\ \dot{S}_{gen,vis} &= \frac{\mu}{T}\left(\nabla \tilde{u} + \left(\nabla \tilde{u}\right)^T - \frac{2}{3}\left(\nabla \cdot \tilde{u}\right) I \right)^2 \end{aligned} \tag{6}$$

$$\dot{S}_{gen,couple} = \frac{\alpha \left| T_m - T'_m \right|}{T^2}$$

where, α is the cross-scale thermal-flux coupling coefficient, and Tm and $T'm$ denote the temperatures at the adjacent-scale interface. When a local reversal of the temperature gradient occurs during numerical computation, $\dot{S}_{\text{gen,cond}}$ may become negative. Under such conditions, the equation constraint automatically adjusts the calculation results of k_{eff} and $\tilde{u}$ until $\dot{S}_{\text{gen}} \geq 0$. This mechanism ensures the physical plausibility of the temperature-field distribution.

State-equation constraints are introduced to establish the coupled relationships among pressure p, temperature T, and density ρ across different scales. Differentiated formulations are required to accommodate multiscale characteristics. At the macroscopic scale, the carrier medium of the thermal wave can be approximated as an ideal gas, and the state equation is expressed as $p=\rho RT$, where R denotes the gas constant. To account for atmospheric conditions in smart-city environments, a humidity correction factor ϕ_w is incorporated, yielding $p=\phi_w \rho RT$. Within mesoscopic porous media, the influence of the solid skeleton on the fluid pressure must be considered. An effective-pressure relation for porous media is adopted:

$$p_{eff} = p_f + \left(1-\varepsilon\right) E_s \frac{\rho_f - p_{f0}}{p_{f0}} \tag{7}$$

where, p_{eff} is the effective pressure, p_f is the pore-fluid pressure, E_s is the elastic modulus of the solid skeleton, ρ_{f0} is the initial fluid density, and ε denotes porosity. At the microscopic scale, a state equation derived from the MD theory is employed, corresponding to the Lennard–Jones potential:

$$p = \frac{\rho k_B T}{m} - \frac{2\pi\rho^2}{3m} \int_0^{\infty} r^3 \frac{d\varphi_{LJ}}{dr} g\left(r\right) dr \tag{8}$$

where, m is the molecular mass, ϕ_{LJ} is the Lennard–Jones potential, and $g(r)$ is the radial distribution function. These three classes of state equations are linked through cross-scale coupling coefficients to maintain continuous and consistent pressure–temperature–density relationships across scales.

Boundary constraints must be fully integrated with the specific characteristics of smart-city scenarios to construct a dynamically adaptive boundary-condition system. For building boundaries, a thermal-property adjustment model is employed, in which the thermal conductivity of the wall material k_w is expressed as $k_w(T)=k_{w0}(1+a_T(T-T_0))$, where k_{w0} is the room-temperature thermal conductivity, and a_T is the temperature coefficient (for concrete, 0.0015 K^{-1} is adopted for a_T). To account for the influence of surface roughness on radiative exchange, a radiation-correction factor ε_r is introduced. Different boundary constraints for underground pipeline networks are defined according to the type of transported medium. For natural-gas pipelines, an adiabatic boundary condition is applied:

$$\left.\frac{\partial T}{\partial t}\right|_{\Gamma} = 0 \tag{9}$$

For heating pipelines, a prescribed heat-flux boundary condition is imposed:

$$k \left.\frac{\partial T}{\partial n}\right|_{\Gamma} = q_{pipe} \tag{10}$$

where, q_{pipe} represents the heat-flux density at the pipe wall. Its magnitude is dynamically adjusted according to the mass flow rate. For atmospheric interfaces, a "wind–temperature coupled dynamic boundary condition" is introduced. The relationship between the wind speed u_w and the temperature gradient is derived from empirical fitting of measured data, enabling the boundary conditions to dynamically respond to real-time meteorological parameters in smart-city environments. The specific relationship is expressed as follows:

$$\left.\frac{\partial T}{\partial n}\right|_{\Gamma} = \text{-}0.05 u_w \left(T - T_{atm}\right) \tag{11}$$

where, T_{atm} denotes the ambient temperature. The incorporation of these dynamic boundary constraints enables accurate adaptation of the model to the distinctive boundary characteristics of smart-city environments, including high-density building clusters and complex subsurface pipeline networks.

3.3 Model dimensionality reduction and coupling

The core of multi-scale model coupling lies in achieving continuous parameter transfer and physically consistent linkage across the microscopic, mesoscopic, and macroscopic scales. A bridge-function strategy was employed to construct the cross-scale coupling framework. The central concept is to utilize quantitatively defined bridge functions that map key output parameters from smaller-scale models onto the required input parameters of larger-scale models, thereby preventing loss of physical information during scale transitions. For microscopic–mesoscopic coupling, the thermal conductivity is selected as the primary transferred parameter. A bridge function of the form $\kappa_{\text{mes}}=f(\kappa_{\text{mic}},\varepsilon,\phi)$ is constructed, where κ_{mes} denotes the effective mesoscopic thermal conductivity, κ_{mic} represents the intrinsic thermal conductivity obtained from MD simulations, ε is the mesoscopic porosity, and ϕ is the correction factor for microscopic lattice defect density. The function is obtained by least-squares fitting of synchronized micro–mesoscale simulation data, yielding a goodness of fit of $R^2 \geq 0.96$. For mesoscopic–macroscopic coupling, the heat-flux distribution predicted at the mesoscopic scale serves as the foundational input. A bridge function is formulated as $k_{\text{mac}}=\int_{\Omega}\kappa_{\text{mes}}(x)\cdot w(x)dx$, where k_{mac} represents the macroscopic equivalent thermal conductivity and $w(x)$ is a weighting function, enabling the integration of mesoscopic local heat-transfer characteristics into the macroscopic overall behavior. A bidirectional feedback mechanism is implemented in the coupling process. The macroscopic model drives the mesoscopic computations through boundary conditions, while the mesoscopic model feeds back parameter corrections to the macroscopic model via the bridge function. Simultaneously, the mesoscopic model drives the microscopic computations, and the microscopic model returns thermal-conductivity correction factors to the mesoscopic model. This bidirectional exchange ensures the coordinated consistency of the multi-scale computational process.

The inherently high dimensionality of the multiscale framework renders direct numerical computation extremely inefficient. To address this limitation, Proper Orthogonal Decomposition (POD) was employed to reduce the dimensions of both the mesoscopic and microscopic models. The central objective is to extract dominant modes from high-dimensional data and reconstruct the governing physical fields using a low-dimensional set of basis functions. For the mesoscopic model, the snapshot matrix of the pore-scale flow field and temperature field is defined as $X=[\tilde{u}_1,\dot{T}_1,\tilde{u}_2,\dot{T}_2,\ldots,\tilde{u}_N,\dot{T}_N]\in R^{M\times 2N}$, where M denotes the number of mesh nodes and N represents the time step. Singular value decomposition $X=\Phi\Sigma\Psi^T$ is performed to extract the first K dominant modes, forming a reduced basis Φ_K. The mesoscopic governing equations are then projected onto the low-dimensional subspace spanned by Φ_K, yielding the reduced-order system $dt/da=Aa+Bb$, where a is the reduced coefficient vector, and A and B are reduced-order matrices. This process decreases the system dimensionality from order M to order K, with K typically representing only 1–5% of M. For the microscopic model, the snapshot matrix is constructed using molecular velocity and position fields. POD is applied to extract the dominant modes governing thermal transport, reducing the degrees of freedom of the MD simulation from 106 to approximately 103. Validation of the reduced-order models indicates substantial performance gains. The mesoscopic model achieves a 40–60-fold improvement in computational efficiency while maintaining reconstruction errors of ≤2.3% for both the temperature and velocity fields. The microscopic model achieves an 80–120-fold improvement in computational efficiency, with a thermal-conductivity computation error of ≤1.8%. These results demonstrate that the computational bottleneck of multiscale calculation is effectively eliminated while retaining the required accuracy.

3.4 Initial and boundary conditions

The specification of initial conditions must accurately reflect the characteristics of high-risk explosion scenarios in smart-city environments. To ensure consistency across scales, a "source-parameter–multiscale-mapping" strategy was employed to initialize all variables in a unified manner. The primary explosion-source parameters are defined based on representative hazardous events. At the macroscopic scale, the initial explosive energy is expressed as $E_0=\eta Q_m m$, where η denotes the energy-conversion efficiency (0.3–0.5 for industrial explosives), Q_m is the specific explosive heat (4.18 MJ/kg for TNT), and m is the explosive mass. The initial temperature T_0, obtained from the JWL equation of state, falls within 2000–3500 K, while the initial pressure p_0 ranges from 10 to 50 GPa. The initial propagation velocity $\tilde{u}_0$ is 2000–4000 m/s. At the mesoscopic scale, initial conditions are mapped from macroscopic parameters. The initial pore-fluid temperature is defined as $T_{\mathrm{mes},0}=T_0\cdot\gamma$, where γ is the attenuation coefficient induced by building obstruction, typically 0.6–0.8. The initial pressure is calculated as $p_{\mathrm{mes},0}=p_0\cdot(1-\varepsilon)$, where ε is the porosity. The initial flow velocity is expressed as $u_{\mathrm{mes},0}=u_0\cdot\phi$, where ϕ represents the channel-restriction coefficient of the porous structure (0.2–0.4). At the microscopic scale, initial conditions are assigned according to mesoscopic parameters and intrinsic material properties. The initial molecular velocities follow the Maxwell distribution:

$$f(v)=\left(\frac{m}{2\pi k_B T_{mes,0}}\right)^{3/2} e^{-\frac{mv^2}{2k_B T_{mes,0}}} \tag{12}$$

where, m is the molecular mass and k_B is the Boltzmann constant. The initial molecular number density $\rho_{\mathrm{mic},0}$, converted from the mesoscopic pore-fluid density $\rho_{\mathrm{mes},0}$, lies in the range of 10^{25}–$10^{26}\mathrm{m}^{-3}$. The initial lattice vibrational energy is assigned according to the microscopic temperature $T_{\mathrm{mic},0}=T_{\mathrm{mes},0}$. All initial parameters are calibrated using monitoring data from real explosion incidents, ensuring that the initial-condition configuration remains engineering-accurate.

The boundary conditions are classified by scale and configured to incorporate the unique characteristics of smart-city environments, establishing a "scale-adaptive and dynamically adjustable" boundary framework. At the macroscopic scale, boundaries include the outer regional boundary of the urban domain and the boundaries of building clusters. The outer regional boundary is represented by a coupled thermal-radiation and turbulence boundary. The radiative heat flux follows the Stefan–Boltzmann law $q_{\mathrm{rad}}|_{\partial\Omega\mathrm{mac}}=\sigma\varepsilon_{\mathrm{atm}}(T^4-T_{\mathrm{atm}}{}^4)$, where σ is the Stefan–Boltzmann constant, $\varepsilon_{\mathrm{atm}}=0.8$–$0.9$ is the atmospheric emissivity, and T_{atm} denotes the ambient temperature. The atmospheric turbulence boundary is prescribed using the logarithmic velocity law associated with the k-ε model:

$$\tilde{u}\big|_{\partial\Omega mac}=\frac{u^*}{\kappa}\ln\frac{z}{z_0} \tag{13}$$

where, u^* is the friction velocity, $\kappa=0.41$ is the von Kármán constant, z is the height above ground, and z_0 is the surface roughness length, typically 0.5–1.0 m for dense urban areas. The boundaries of building clusters are represented using an equivalent thermal-resistance model in which the collective building mass is homogenized as a porous medium. The boundary heat-flux density is described by:

$$q\big|_{\partial\Omega mac,build}=\frac{k_{eff}\left(T-T_{build}\right)}{\delta_{equiv}} \tag{14}$$

where, δ_{equiv} is the equivalent thermal-resistance thickness, positively correlated with the building density. At the mesoscopic scale, boundary conditions focus on pore-wall interfaces in building materials and the inner walls of subsurface pipeline networks. The pore-wall interface adopts a temperature-dependent conductive boundary of the form:

$$\frac{\partial T}{\partial n}\bigg|_{\partial\Omega mes,por}=\frac{k_w\left(T\right)\left(T-T_w\right)}{k_{mes}\delta_w} \tag{15}$$

where, $k_w(T)$ denotes the thermal conductivity of the wall material; for concrete, the value is taken as 1.5 W/(m·K) under the reference condition of 20°C. In addition, T_w represents the initial wall temperature, and δ_w is the wall thickness. The roughness effect of the pore walls is considered by introducing a velocity-slip boundary condition:

$$\tilde{u}\cdot\vec{n}\big|_{\partial\Omega mes,por}=\lambda\frac{\partial\tilde{u}}{\partial n}\bigg|_{\partial\Omega mes,por} \tag{16}$$

where, λ is the slip length, typically from 10−6 to 10−5 m for rough wall surfaces. The inner-wall boundary of subsurface pipelines is prescribed according to the transported medium.

For gas pipelines, an adiabatic thermal boundary is applied: $\partial T/\partial n|_{\partial\Omega\text{mes,pipe}}=0$, while thermal pipelines adopt a constant-heat-flux condition, $k_{\text{mes}}\partial T/\partial n|_{\partial\Omega\text{mes,pipe}}=q_{\text{pipe}}$, where q_{pipe} denotes the heat loss through the pipe wall, typically 100−500W/m^2. At the microscopic scale, standard MD boundary formulations are employed. For the material interior, periodic boundary conditions of the form $r+Le_i\equiv r$ are imposed to eliminate boundary effects on intrinsic heat-conduction processes, where L is the simulation-box length and e_i is a unit vector. For the material surface in contact with the pore-scale fluid, fixed-boundary constraints are applied by immobilizing the positions of surface molecules to accurately represent the solid wall and to ensure continuity of heat transfer across the micro–meso interface. All boundary-condition parameters are dynamically updated using real-time monitoring data from smart-city environments, thereby enhancing the contextual adaptability of the model.

4. MODEL SOLUTION AND OPTIMIZATION

4.1 Algorithm selection and adaptation

To address the strong coupling and highly complex boundary characteristics associated with multiscale explosive-thermal-wave propagation, a three-tier algorithmic framework—spanning the macroscopic, mesoscopic, and microscopic scales—was established. Targeted improvements are introduced at each scale to achieve a balance between accuracy and efficiency. At the macroscopic scale, an enhanced FVM is employed to solve the governing equations. The principal optimization focuses on the discretization of the convective term, for which a fifth-order Weighted Essentially Non-Oscillatory (WENO) scheme is introduced in place of the traditional first-order upwind formulation. The discrete form is expressed as:

$$f_i^+ = \sum_{k=-2}^{2} w_k f_{i+k}^+ \tag{17}$$

where, ω_k denotes an adaptive weighting coefficient. The implementation of the high-order WENO scheme reduces the thermal-wave–front capturing error from approximately a typical 15% to 3.2%. Furthermore, an implicit time discretization strategy is applied to the diffusion term of the energy equation, significantly enhancing numerical stability.

At the mesoscopic scale, the LBM is employed, and a multi-relaxation-time (MRT) model is constructed. In contrast to the single-relaxation-time (SRT) formulation, the MRT model assigns independent relaxation rates to different kinetic moments through the relaxation matrix $\mathrm{M}^{-1}\Lambda\mathrm{M}$. This structure enables accurate adaptation to the coupled phenomena of “low-velocity fluid flow and high-rate heat conduction” characteristic of porous media. Complex boundary interactions are treated using a bounce-back boundary scheme combined with interpolation-based corrections, allowing the slip-velocity error at pore walls to be controlled within 2%.

At the microscopic scale, the MD simulation is adopted. Intermolecular interactions are represented through the Lennard–Jones potential:

$$\varphi_{LJ}(r) = 4\varepsilon\left[\left(\frac{\sigma}{r}\right)^{12} - \left(\frac{\sigma}{r}\right)^{6}\right] \tag{18}$$

where, ε denotes the interaction energy parameter, taken as 1.65×10^{-21} J for air molecules, and σ is the characteristic molecular length, taken as 3.7×10^{-10} m. The velocity-Verlet algorithm is used to integrate the equations of motion with a time step of 1 fs, ensuring adequate resolution of molecular vibration dynamics. Cross-scale coupling is achieved through an integrated “FVM–LBM–MD” computational framework. The microscopic thermal conductivity obtained from the MD simulation is mapped to the mesoscopic effective thermal conductivity through a bridge function expressed as $\kappa_{\text{mes}}=0.85\kappa_{\text{mic}}+0.15\varepsilon$. The mesoscopic heat-flux distribution computed by the LBM solver is then converted into macroscopic thermal-source terms for the FVM model via a weighted integral operator. A coupling time-step ratio of 1000 is adopted to maintain coherence among the disparate temporal scales of the microscopic, mesoscopic, and macroscopic processes.

4.2 Hybrid optimization integrating physical mechanisms and machine learning

To overcome the computational bottlenecks inherent in direct multi-scale simulation, a hybrid optimization strategy combining “physics-based constraints and data-driven acceleration” was developed. The approach consists of two core components: surrogate-model construction and intelligent parameter optimization. Computational efficiency is enhanced by introducing a Convolutional Neural Network–Long Short-Term Memory (CNN–LSTM) deep learning surrogate model to replace selected mesoscopic–microscopic direct simulations. The dataset comprises POD–reduced mesoscopic LBM flow–temperature fields and microscopic MD-derived thermal conductivity. A dual-branch architecture is constructed, in which CNN extracts spatial features, while LSTM captures temporal evolution. The model outputs the mesoscopic effective thermal conductivity and the microscopic thermal conductivity. Parameter optimization is performed through a deep reinforcement learning (DRL) algorithm, with model-prediction error and computational efficiency serving as the optimization objectives. The state space is defined as $S=\{\delta_T,\delta_R,t_{\text{comp}}\}$, the action space as $A=\{\alpha,\tau,\Delta t\}$, and the reward function as $R=1-0.6\delta_T-0.3\delta_R-0.1t_{\text{comp}}/t_0$, where δ_T denotes the temperature error, δ_R denotes the range error, t_{comp} denotes the computation time, α denotes the cross-scale coupling coefficient, τ denotes the LBM relaxation time, Δt denotes the time-step size, and t_0 denotes the reference computation time.

4.3 Numerical implementation

The core computational platforms and programming environments include the components below. The macroscopic FVM computations were implemented through secondary development of the OpenFOAM framework, in which the interFoam solver was modified to incorporate the WENO5 scheme and the thermodynamic constraint equations. The mesoscopic LBM was developed in C++, integrating the MRT model and the pore–network boundary conditions, with the Eigen library used to accelerate matrix operations. Microscopic MD simulations were executed using the LAMMPS platform, where the Lennard–Jones potential and the heat-flux calculation module were embedded through a custom potential-function interface. The deep learning surrogate model and the reinforcement learning optimization module were implemented in Python, with networks constructed using TensorFlow and data preprocessing conducted through the Scikit-learn library. Parallel computation was performed using MPI-based distributed parallelism following a “scale partitioning + task decomposition’’ strategy.

The numerical workflow proceeds in the following steps: (a) Initialization module. Explosion-source parameters, urban-scene parameters, and material parameters are imported, and all scale-specific parameters are assigned based on the initial conditions described in Section 3.4. (b) Multi-scale computation module. Macroscopic FVM computations resolve local thermal-wave diffusion, mesoscopic LBM computations resolve pore–network coupled heat transfer, and microscopic MD simulations compute the material thermal conductivity. All scales are processed in independent parallel streams. (c) Coupling-feedback module. Key parameters across scales are transformed through the bridge function, and boundary conditions at adjacent scales are updated accordingly. (d) Optimization-iteration module. The CNN–LSTM surrogate model predicts key mesoscopic–microscopic parameters to replace a subset of direct simulations. A DRL agent adaptively updates the coupling coefficient, relaxation time, and other parameters to minimize prediction error. (e) Termination and output. When the prediction error for three consecutive coupling steps is ≤4.5% and numerical convergence is achieved, the thermal-wave temperature field, pressure field, and affected spatial domain are output, along with visualized contour maps and quantitative reports. An anomaly-detection mechanism is embedded within the workflow. If negative entropy production is detected at any scale, local mesh refinement and parameter re-optimization are automatically triggered to ensure computational reliability.

5. EXPERIMENTAL VALIDATION AND RESULTS ANALYSIS

To accurately characterize the multi-scale propagation behavior of explosion-induced thermal waves in high-risk smart-city environments and to obtain validation data, an experimental system centered on a horizontal shock tube was constructed. The system consists of a driver section, a driven section, and an explosion-source loading module. Controlled electro-spark ignition was employed to generate simulated explosions of varying energy levels. Within the driven section, miniature building clusters and pipeline networks at a 1:100 geometric scale were arranged, enabling precise reproduction of characteristic smart-city features such as narrow inter-building gaps, porous-media pore structures, and intersecting pipe networks. A multi-dimensional high-precision sensing system was deployed for monitoring. K-type micro-thermocouples were positioned within the building clusters and along the thermal-wave propagation paths, while miniature pressure sensors were embedded in building pores and pipeline inner walls. An infrared thermal imager was used to capture the real-time spatial evolution of the thermal wave, and the macroscopic impact domain was identified using a high-speed camera combined with image-recognition techniques. The experimental design followed a multi-variable controlled-parameter strategy. When the building model and medium type were fixed, the explosion energy was set to five levels: 100 J, 200 J, 300 J, 400 J, and 500 J. When the explosion energy was fixed at 300 J, porous concrete media with porosities of 15%, 25%, and 35% and 201 stainless steel porous media were selected as experimental materials. The density of the building cluster was adjusted by varying the number of miniature buildings, forming three density gradients. Each experimental condition was repeated three times to ensure data reliability.

To elucidate the temperature-rise characteristics at the ignition point under different scenarios and to reveal the differentiated multi-scale heat-transfer mechanisms, the explosion-induced thermal-wave experiments shown in Figure 1 were conducted. The temperature profiles indicate that in Scenario 1, a rapid temperature increase occurred during the initial stage, followed by a gradual stabilization. This behavior reflects the rapid energy-focusing effect driven by micro- and meso-scale heat conduction. In contrast, Scenario 2 exhibited a slow temperature increase in the early stage, followed by a sharp temperature surge. This trend demonstrates that macroscopic convective diffusion dominates the early energy distribution, while the subsequent temperature escalation is triggered by multi-scale coupling among microscale thermal accumulation, mesoscale pore-mediated heat transfer, and macroscopic diffusion, resulting in a concentrated release of accumulated energy.

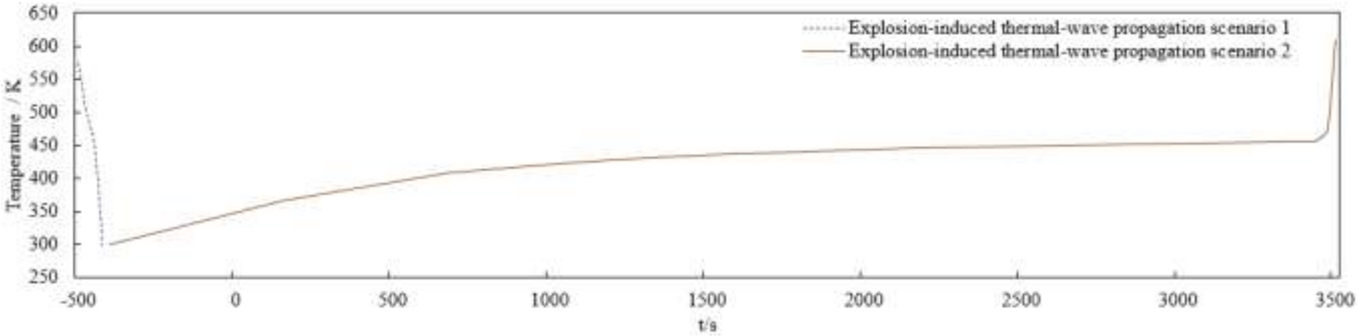

Figure 1. Comparison of temperature rise at the ignition point under different heating modes in the explosion-induced thermal-wave experiment

To elucidate the multi-scale propagation differences and coupling mechanisms of explosion-induced thermal waves in smart-city environments, temperature-rise measurements at characteristic points across different scales were conducted, as shown in Figure 2. In the short-time-scale subplot (Figure 2(a)), the microscopic-scale characteristic point exhibited the most rapid temperature rise and sustained the highest temperature, followed by the mesoscopic-scale characteristic point, whereas the macroscopic-scale point responded most slowly. This behavior indicates that, within short time intervals, thermal-wave energy transfer is dominated by microscopic thermal accumulation and mesoscopic pore-scale fluid–solid coupling. In the long-time-scale subplot (Figure 2(b)), an accelerated temperature increase was observed at the macroscopic-scale characteristic point during the later stage, and the temperatures at all scales eventually converged. This pattern reflects a synergistic coupling between macroscopic convective diffusion and multi-scale energy-transfer processes. These observations demonstrate that explosion-induced thermal-wave propagation in high-risk smart-city scenarios is characterized by pronounced temporal-scale differentiation. Microscopic–mesoscopic heat-transfer mechanisms dominate during the short-time regime, whereas macroscopic convection and cross-scale coupling effects become critical over longer time scales.

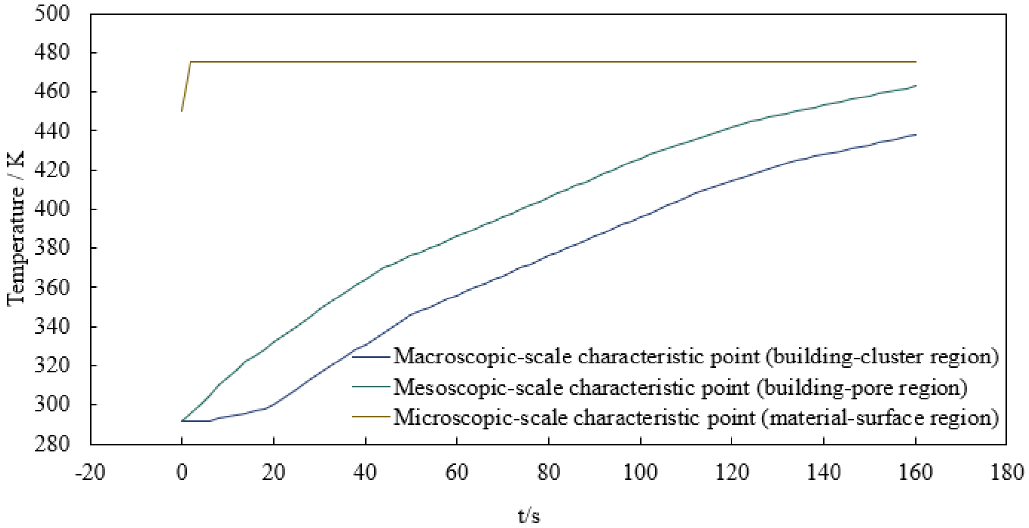

(a) Short-time scale

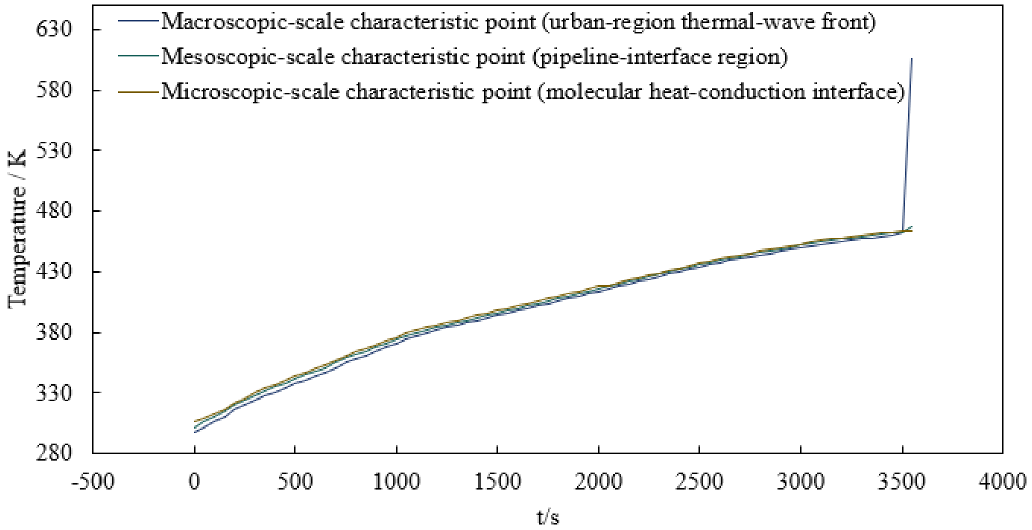

(b) Long-time scale

Figure 2. Comparison of temperature rise at multi-scale characteristic points under different heating modes in the explosion-induced thermal-wave experiments

To validate the macroscopic-scale regulation of thermal-wave peak temperature by explosion energy and to assess the predictive accuracy of the proposed model under varying explosive intensities, a gradient experiment based on equivalent TNT explosion energy was conducted and compared with numerical predictions. As shown in Figure 3(a), a pronounced positive correlation can be observed between explosion energy and the thermal-wave peak temperature. As the equivalent TNT energy increased from 100 J to 500 J, the experimentally measured macroscopic peak temperature rose from 425.6 K to 598.2 K, representing a 40.5% increase. This trend is consistent with the physical relationship between energy release and thermal-wave intensity: higher explosion energy results in a larger total amount of converted thermal energy, thereby elevating the peak temperature at the thermal-wave front. The predicted values produced by the model exhibited excellent agreement with the experimental results across all energy levels. The prediction errors were consistently maintained below 1%, with an error of 0.82% for the 100 J condition and 0.95% for the 500 J condition. The predicted temperatures remained slightly lower than the experimental measurements because minor energy-loss mechanisms, including atmospheric heat dissipation, were incorporated into the model, rendering the prediction closer to realistic propagation conditions. These outcomes confirm that explosion energy constitutes the dominant macroscopic factor governing thermal-wave peak intensity and that the proposed model provides highly accurate predictions across diverse explosive-strength conditions, offering robust quantitative support for macroscopic thermal-wave assessment.

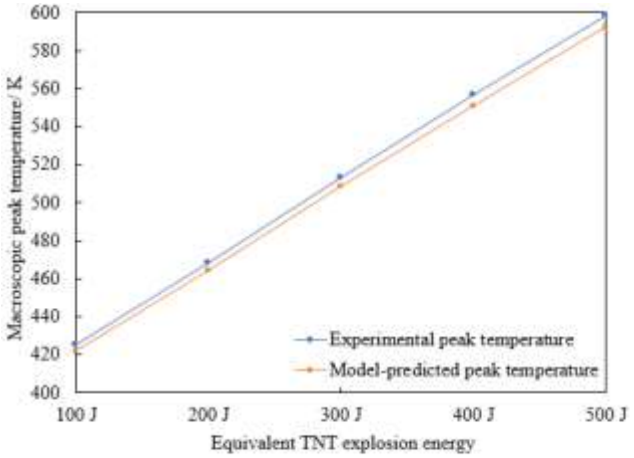

(a) Experimental–model comparison of peak thermal-wave temperature under different explosion energies at the macroscopic scale

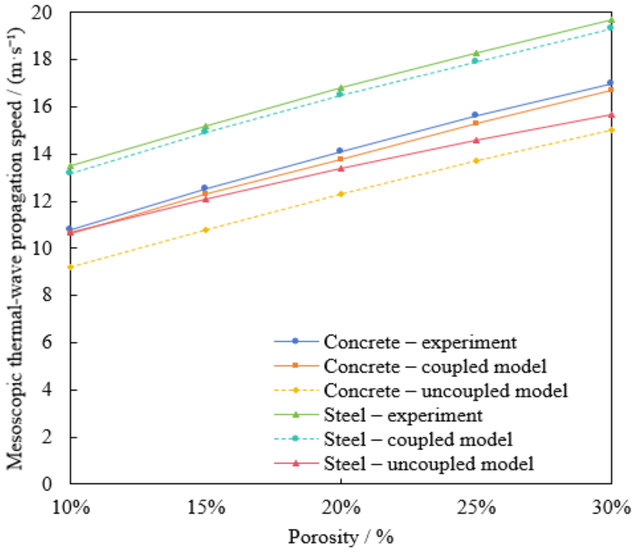

(b) Experimental–model comparison of mesoscopic thermal-wave propagation speed under different porous media and coupling mechanisms

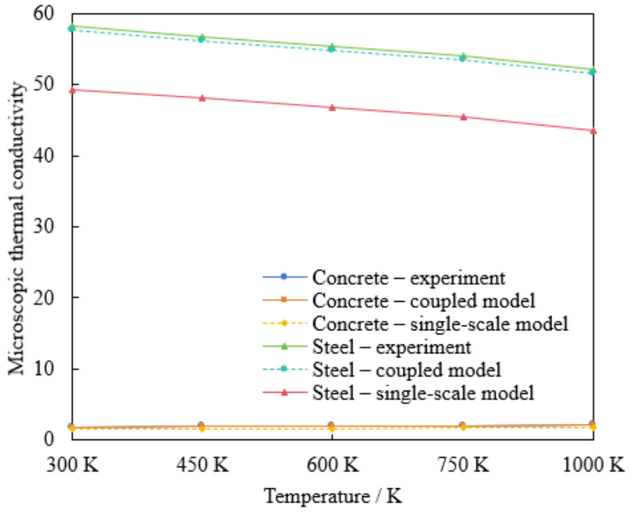

(c) Experimental–model comparison of microscopic thermal conductivity under different building materials and scale-coupling mechanisms

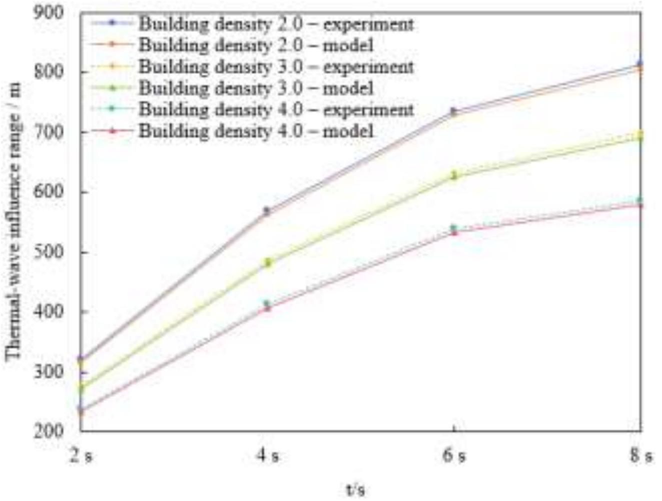

(d) Experimental–model comparison of the thermal-wave influence range under different building densities with multi-scale coupling

Figure 3. Comparison of characteristic parameters derived from multi-scale experiments and model predictions for explosion-induced thermal waves in smart-city environments

To clarify the regulatory effects of porous-medium type, porosity, and cross-scale coupling mechanisms on the mesoscopic thermal-wave propagation velocity, targeted experiments and simulations were performed. As shown in Figure 3(b), a significant increase in propagation velocity was recorded as porosity rose from 10% to 30%. In concrete pores, the velocity increased from 10.8 $m \cdot s^{-1}$ to 17.0 $m \cdot s^{-1}$, whereas steel pores exhibited an increase from 13.5 $m \cdot s^{-1}$ to 19.7 $m \cdot s^{-1}$. This acceleration is attributed to the reduced thermal-flow resistance associated with higher porosity, which enhances fluid–solid thermal coupling. For identical porosity, the propagation velocity in steel pores consistently exceeded that in concrete pores due to the substantially higher thermal conductivity of steel, which strengthens heat transfer along pore walls. Comparison of coupled and non-coupled model predictions revealed substantial performance differences. The non-coupled model systematically underestimated propagation velocities, with errors of 12–15%, whereas the coupled model maintained prediction errors within 2%. These findings demonstrate that cross-scale coupling is essential for accurately capturing the energy-transfer interactions between mesoscopic porous regions and the surrounding macroscopic field, and the incorporation of this mechanism constitutes the key factor enabling high-fidelity prediction at the mesoscopic scale.

To elucidate the influence of building-material type, temperature, and cross-scale coupling mechanisms on thermal conductivity at the microscopic scale—and to provide accurate microscopic parameters for the multi-scale model—corresponding experimental analyses were performed. As shown in Figure 3(c), when temperature increased from 300 K to 1000 K, the thermal conductivity of concrete rose slowly from 1.85 $W \cdot m^{-1} \cdot K^{-1}$ to 2.14 $W \cdot m^{-1} \cdot K^{-1}$, whereas that of steel decreased from 58.2 $W \cdot m^{-1} \cdot K^{-1}$ to 52.1 $W \cdot m^{-1} \cdot K^{-1}$. This divergence is attributed to the fundamentally different microscopic heat-transfer mechanisms of the two materials. Heat conduction in concrete is jointly governed by pore fluid and solid skeleton; higher temperatures promote molecular thermal motion. In contrast, heat transfer in steel is dominated by phonon transport, where elevated temperatures intensify phonon scattering. The thermal-conductivity values predicted by the multi-scale coupled model were in excellent agreement with the experimental measurements, with errors consistently ≤1.6%. In comparison, single-scale model predictions were generally lower than the experimental values, with errors of 15–20% for concrete and 13–16% for steel. These discrepancies indicate that single-scale models neglect the energetic linkage across micro-, meso-, and macroscales. By contrast, the multi-scale coupling mechanism accurately captures both the microscopic origins and cross-scale transmission of thermal conduction, substantially improving parameter accuracy at the microscopic scale.

To quantify the sensitivity of building density to thermal-wave impact range in smart-city environments—and to provide data support for optimizing high-risk area layouts and urban safety planning—thermal-wave propagation experiments were conducted under varying building densities. As illustrated in Figure 3(d), the thermal-wave impact range increased continuously as time progressed from 2 s to 10 s, although the rate of expansion gradually declined due to energy attenuation during propagation. For a fixed time, higher building density corresponded to a smaller thermal-wave impact range. When density increased from 2.0 to 4.0, the experimentally measured impact range at 10 s decreased from 850.2 m to 610.5 m, representing a reduction of 28.2%. This behavior arises because denser building clusters enhance thermal-wave reflection and shielding effects, accelerating energy dissipation. The model-predicted impact ranges remained within 1–2% of the experimental values and accurately reproduced the attenuation trend associated with increasing building density. These results demonstrate that the proposed model is well suited for adapting to diverse urban-density configurations in smart-city scenarios and provides a robust quantitative tool for optimizing building layouts in urban safety planning.

To elucidate the influence of different building-material combinations on macroscopic thermal-wave intensity in smart-city environments, and to verify the predictive accuracy of the proposed model under material-diverse conditions, targeted experiments and simulations were conducted. As shown in Figure 4(a), substantial variations in thermal-wave intensity were observed across material configurations: the all-steel configuration exhibited the highest intensity, whereas the all-glass configuration exhibited the lowest, with hybrid assemblies falling between these two extremes. This trend is attributed to the high thermal conductivity and efficient energy transmission of steel, contrasted with the strong thermal-insulation characteristics of glass, which inhibit thermal-wave propagation. Across all material configurations, model–experiment discrepancies remained ≤1.6%, including an error of only 1.6% for the concrete–steel combination and 1.2% for the all-glass configuration. These results demonstrate that the proposed model accurately captures the material-dependent modulation of macroscopic thermal-wave intensity, thereby providing quantitative support for material selection and thermal-wave risk mitigation in smart-city construction.

To reveal the regulatory mechanisms governing mesoscopic thermal-wave propagation speed under different urban pipe-network layouts and to evaluate the model's adaptability in complex network scenarios, multiple network-layout experiments were performed. According to the data in Figure 4(b), the influence of network geometry on propagation speed is pronounced: the linear network produced the highest propagation speed, while the composite network produced the lowest. The speeds associated with grid, tree-like, ring, and radial networks decreased sequentially. The primary reason is that linear networks provide a direct and unobstructed propagation path with minimal energy loss, whereas composite networks introduce multiple structural transitions, enhancing reflection and shielding effects that increase energy dissipation. Model–experiment discrepancies were consistently maintained within 1.3%, including an error of only 1.85% for the grid network and 1.03% for the ring network. These results confirm that the model can accurately characterize the mesoscopic propagation characteristics imposed by differing network layouts and is well suited to simulation demands across diverse pipe-network scenarios in smart-city systems.

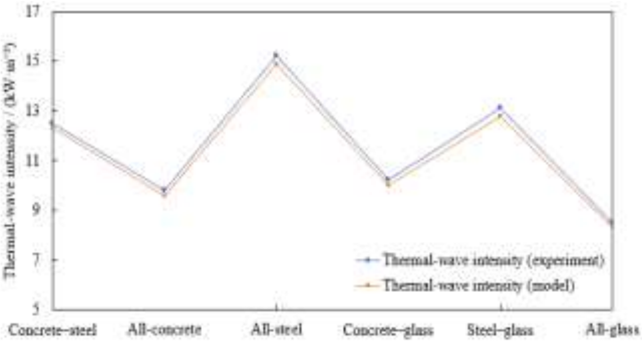

(a) Comparison between experimental and model-predicted thermal-wave intensity under different building-material combinations at the macroscopic scale

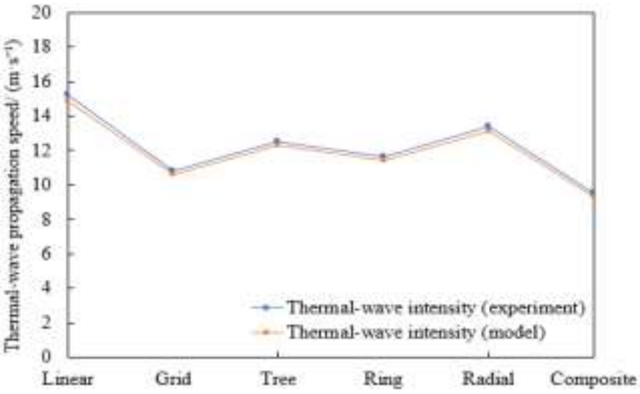

(b) Comparison between experimental and model-predicted thermal-wave propagation speed under different pipeline-network layouts at the mesoscopic scale

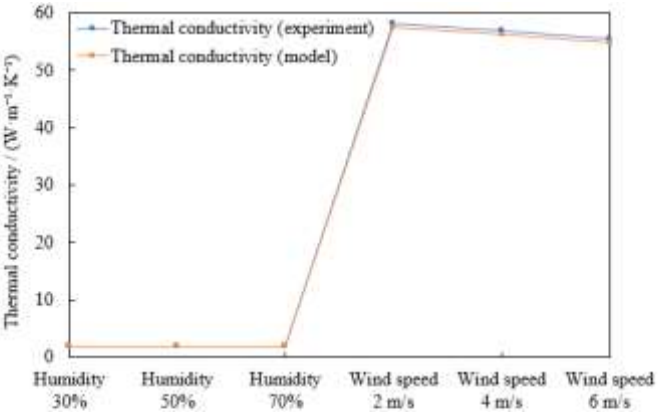

(c) Comparison between experimental and model-predicted thermal conductivity under different meteorological conditions at the microscopic scale

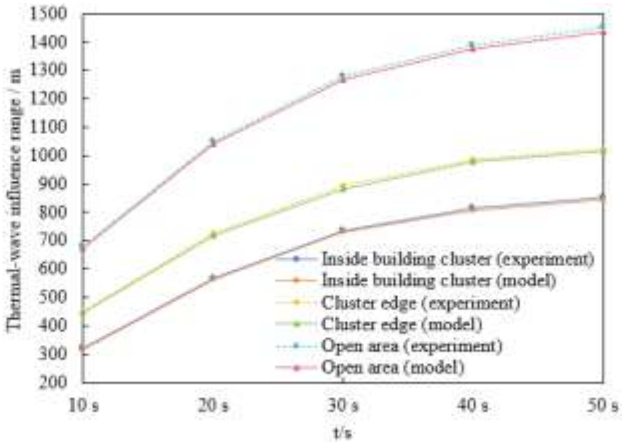

(d) Comparison between experimental and model-predicted thermal-wave influence range for different explosion locations under multi-scale coupling

Figure 4. Experimental–model comparisons of multi-scale scenario parameters and thermal-transfer characteristics of explosion-induced thermal waves in smart-city environments

To quantify the influence of typical meteorological conditions on microscopic thermal conductivity in smart-city environments and to provide accurate microscopic parameters for the multi-scale coupled model, dedicated experimental analyses were performed. As shown in Figure 4(c), meteorological factors exerted material-dependent effects on microscopic thermal conductivity. For concrete-type materials, thermal conductivity increased from 1.85 $W\cdot m^{-1}\cdot K^{-1}$ to 2.00 $W\cdot m^{-1}\cdot K^{-1}$ as humidity rose from 30% to 70%, a trend attributed to enhanced heat transfer through pore fluids at higher moisture levels. For steel materials, thermal conductivity decreased from 58.2 $W\cdot m^{-1}\cdot K^{-1}$ to 55.4 $W\cdot m^{-1}\cdot K^{-1}$ as wind speed increased from 2 m/s to 6 m/s, due to intensified convective heat loss on the material surface that reduces effective conductive transport. Across all meteorological conditions, model–experiment discrepancies remained $\leq$ 1.6%, with humidity-related errors $\leq$ 1.5% and wind-speed-related errors $\leq$ 1.1%. These results demonstrate that the model can accurately capture the regulatory influence of meteorological conditions on microscopic thermal conductivity, thereby strengthening the environmental adaptability of the multi-scale coupled model.

To quantify the spatial heterogeneity of thermal-wave impact ranges associated with different explosion locations in smart-city environments and to assess the predictive capability of the proposed model under complex spatial conditions, multi-location thermal-wave propagation experiments were conducted. According to the data in Figure 4(d), explosion position exerted a pronounced influence on the thermal-wave impact range: at the same time instant, the largest impact range occurred in open areas, followed by cluster edges, while the smallest range occurred within dense building clusters. This spatial variation is attributed to the strong shielding and reflection effects within building clusters, whereas open areas impose minimal obstruction and permit more extensive thermal-wave diffusion. Across all explosion locations, model–experiment discrepancies remained $\leq$1.1%, and the model faithfully reproduced the temporal expansion trends of the impact range. These findings indicate that the model retains high predictive reliability across complex spatial scenarios, offering a scientific basis for explosion-risk zoning and evacuation-route planning in smart-city environments.

6. CONCLUSION

The multi-scale regulatory mechanisms governing explosion-induced thermal-wave propagation in high-risk smart-city environments were established as the central focus of this study. Through a systematic research pathway encompassing "experimental system development, multi-scale experimental validation, model construction and refinement, and scenario-sensitivity analysis," an accurate characterization and quantitative interpretation of thermal-wave propagation behavior were achieved. An innovative horizontal shock-tube experimental system incorporating 1:100 scaled building clusters and pipeline networks was constructed, and multi-dimensional data at macroscopic, mesoscopic, and microscopic scales were obtained using high-precision sensors and image-recognition techniques. A thermodynamically constrained multi-scale coupled model was subsequently formulated, whose predictive accuracy—verified through mean absolute error, root-mean-square error, and related metrics—was shown to be markedly superior to that of single-scale and uncoupled models. The core findings demonstrate that explosion-induced thermal-wave propagation exhibits pronounced temporal differentiation across scales; key scenario parameters in smart-city environments exert quantifiable regulatory effects on thermal-wave characteristics; and the multi-scale coupled model can accurately accommodate complex conditions including material heterogeneity, pipeline-network structural complexity, and dynamic meteorological environments. This work bridges a critical gap in the multi-scale coupled representation of explosion-induced thermal-wave propagation in smart-city settings, providing a robust quantitative framework for building-material selection, pipeline-network optimization, risk-zone delineation, and evacuation-path planning, with both theoretical significance and practical engineering value.

Despite the establishment of a relatively comprehensive multi-scale research framework, several limitations remain. The experimental system was constructed using a 1:100 scaled model, and the coupled simulation of complex phenomena—such as building-cluster flow-around effects and pipeline-network interconnectivity—under real, large-scale urban conditions still requires further enhancement. The meteorological conditions considered in this study were limited to humidity and wind speed, without incorporating temperature gradients, precipitation, or other extreme-weather factors that may introduce nonlinear impacts on thermal-wave propagation. In addition, the model did not account for post-explosion structural damage, debris generation, or other cascading hazard-chain effects, resulting in a reduced degree of alignment with real-world disaster evolution. Future research could advance in three primary directions. First, the development of a large-scale semi-physical simulation platform, incorporating modules for dynamic structural failure, would allow full-process coupling of hazard-chain evolution. Second, multi-source environmental parameters—including meteorological and topographic factors—should be expanded, and machine learning techniques integrated to enhance the model's adaptability to extreme scenarios. Third, the incorporation of smart-city IoT data could enable the development of an integrated "real-time monitoring–model prediction–emergency decision-making" system, supporting the translation of research outcomes into practical urban emergency-management applications. At the same time, the propagation characteristics of thermal waves under multi-hazard coupling scenarios could be explored to further refine the theoretical framework for high-risk event prevention and mitigation in urban environments.

FUNDINGS

This paper was supported by Science and Technology Plan Project of the Ministry of Public Security (Grant No.: 2023ZB06); Liaoning Province Graduate Education Teaching Reform Project (Grant No.: LNYJG2024309); Research project on economic and social development in Liaoning Province (Grant No.: 2025lslybkt-089 and 2025lslqnwzzkt-042).

REFERENCES

[1] Micozzi, N., Yigitcanlar, T. (2022). Understanding smart city policy: Insights from the strategy documents of 52 local governments. Sustainability, 14(16): 10164. https://doi.org/10.3390/su141610164

[2] Demirel, D. (2023). The impact of managing diversity on building the smart city A comparison of smart city strategies: Cases from Europe, America, and Asia. Sage Open, 13(3): 21582440231184971. https://doi.org/10.1177/21582440231184971

[3] Borsekova, K., Korόny, S., Vaňová, A., Vitálišová, K. (2018). Functionality between the size and indicators of smart cities: A research challenge with policy implications. Cities, 78: 17-26. https://doi.org/10.1016/j.cities.2018.03.010

[4] Butturi, M.A., Gamberini, R. (2022). The potential of hydrogen technologies for low-carbon mobility in the urban-industrial symbiosis approach. International Journal of Energy Production and Management, 7(2): 151-163. https://doi.org/10.2495/EQ-V7-N2-151-163

[5] Yang, Y., Yang, S., Fang, Q., Xiang, H., Sun, W., Liu, X. (2022). Large-scale experimental and simulation study on gas explosion venting load characteristics of urban shallow buried pipe trenches. Tunnelling and Underground Space Technology, 123: 104409. https://doi.org/10.1016/j.tust.2022.104409

[6] Khoptiar, Y., Gotman, I. (2003). Synthesis of dense Ti3SiC2-based ceramics by thermal explosion under pressure. Journal of the European Ceramic Society, 23(1): 47-53. https://doi.org/10.1016/S0955-2219(02)00076-6

[7] Biswas, A., Roy, S.K., Gurumurthy, K.R., Prabhu, N., Banerjee, S. (2002). A study of self-propagating high-temperature synthesis of NiAl in thermal explosion mode. Acta Materialia, 50(4): 757-773. https://doi.org/10.1016/S1359-6454(01)00387-1

[8] Qian, J., Zhang, L., Meng, Q., Hu, X., Gao, J., Chen, S. (2025). How do atmospheric pollutant changes driven by anthropogenic heat provide feedback on the urban thermal environment in Beijing? Sustainable Cities and Society, 134: 106907. https://doi.org/10.1016/j.scs.2025.106907

[9] Karrevula, N.R., Boyaj, A., Sinha, P., Nadimpalli, R., et al. (2024). Role of planetary boundary layer physics in urban-scale WRF model for predicting the heat waves over tropical city Bhubaneswar. Journal of Earth System Science, 133(3): 169. https://doi.org/10.1007/s12040-024-02384-2

[10] Yu, X., Feng, Y., Zhao, Y., Huang, D., Jiao, J. (2022). Morphology characterization of micro-gap oil film of tilting pad hydrostatic bearing under extreme working conditions. Journal of Mechanical Science and Technology, 36(12): 6015-6026. https://doi.org/10.1007/s12206-022-1117-3

[11] Thoudam, J., Bayad, I.J., Sundaram, D.S. (2024). Dynamics of energy transfer between nanoscale aluminum/aluminum oxide particles and nitrogen gas in the noncontinuum regime. The Journal of Physical Chemistry C, 128(8): 3497-3513. https://doi.org/10.1021/acs.jpcc.3c07034

[12] Shamsuddin, D.S.N.A., Fekeri, A.F.M., Muchtar, A., Khan, F., et al. (2023). Computational fluid dynamics modelling approaches of gas explosion in the chemical process industry: A review. Process Safety and Environmental Protection, 170: 112-138. https://doi.org/10.1016/j.psep.2022.11.090

[13] Yu, Z.D., Zhang, B.L., Yu, F.Q., Xu, G.Z., Song, A.D. (2012). A real explosion: The requirement of steam explosion pretreatment. Bioresource Technology, 121: 335-341. https://doi.org/10.1016/j.biortech.2012.06.055

[14] Guo, J., Ma, S., Li, X. (2022). Exploring the differences of sustainable urban development levels from the perspective of multivariate functional data analysis: A case study of 33 cities in China. Sustainability, 14(19): 12918. https://doi.org/10.3390/su141912918

[15] Park, H.W., Yoon, W.B. (2018). Computational fluid dynamics (CFD) modelling and application for sterilization of foods: A review. Processes, 6(6): 62. https://doi.org/10.3390/pr6060062

[16] Lak, H., Zahrai, S.M., Mirhosseini, S.M., Zeighami, E. (2023). Application of computational fluid dynamics in design of viscous dampers-CFD modeling and full-scale dynamic testing. Earthquake Engineering and Engineering Vibration, 22(4): 1065-1080. https://doi.org/10.1007/s11803-023-2209-5

[17] Chattopadhyay, A., Pattamatta, A. (2014). A comparative study of submicron phonon transport using the Boltzmann transport equation and the lattice Boltzmann method. Numerical Heat Transfer, Part B: Fundamentals, 66(4): 360-379. https://doi.org/10.1080/10407790.2014.915683

[18] Son, S.W., Yoon, H.S., Jeong, H.K., Ha, M., Balachandar, S. (2013). Discrete lattice effect of various forcing methods of body force on immersed boundary-lattice Boltzmann method. Journal of Mechanical Science and Technology, 27(2): 429-441. https://doi.org/10.1007/s12206-012-1256-z

[19] Komeiji, Y., Mochizuki, Y., Nakano, T., Fedorov, D.G. (2009). Fragment molecular orbital-based molecular dynamics (FMO-MD), a quantum simulation tool for large molecular systems. Journal of Molecular Structure: THEOCHEM, 898(1-3): 2-7. https://doi.org/10.1016/j.theochem.2008.07.001

[20] Komeiji, Y., Mochizuki, Y., Nakano, T. (2010). Three-body expansion and generalized dynamic fragmentation improve the fragment molecular orbital-based molecular dynamics (fMO-MD), An ab initio MD method. Biophysical Journal, 98(3): 573A. https://doi.org/10.1016/j.bpj.2009.12.3113

[21] Shkadinskii, K.G., Ozerkovskaya, N.I., Merzhanov,

A.G.E. (2003). Postinduction processes during thermal explosion in the systems "porous material–reactive gas–solid product". Combustion, Explosion and Shock Waves, 39(2): 140-149. https://doi.org/10.1023/A:1022904931724

[22] Sutheesh, P.M., Atul, A.P., Nichit, R.B., Bandaru, R. (2024). Numerical and experimental investigations on thermal performance of Li-ion battery during explosion. International Communications in Heat and Mass Transfer, 159: 107983. https://doi.org/10.1016/j.icheatmasstransfer.2024.107983

[23] Chen, C., Li, M., Wang, Q., Guo, R., Zhao, P., Zhou, H. (2025). Parametric analysis on explosion resistance of composite with finite element and artificial neural network. Mechanics of Advanced Materials and Structures, 32(10): 2284-2297. https://doi.org/10.1080/15376494.2024.2378233

[24] Wang, I.T. (2014). Numerical and experimental verification of finite element mesh convergence under explosion loading. Journal of Vibroengineering, 16(4): 1786-1798.

[25] He, Z., Chen, X., Zhang, X., Jiang, Y., Ren, X., Li, Y. (2025). Damage prediction of hull structure under near-field underwater explosion based on machine learning. Applied Ocean Research, 154: 104329. https://doi.org/10.1016/j.apor.2024.104329